Journal of
Materials Chemistry C

Materials for optical, magnetic and electronic devices

Accepted Manuscript

This article can be cited before page numbers have been issued, to do this please use: M. Crozzolin, C. Belloni, J. Xu, T. Nakanishi, J. Ueda, S. Tanabe, F. Dallo, E. Balliana, A. Saorin, F. Rizzolio, D. Cristofori, P. Riello, A. Benedetti and M. Back, *J. Mater. Chem. C*, 2024, DOI: 10.1039/D4TC01386G.

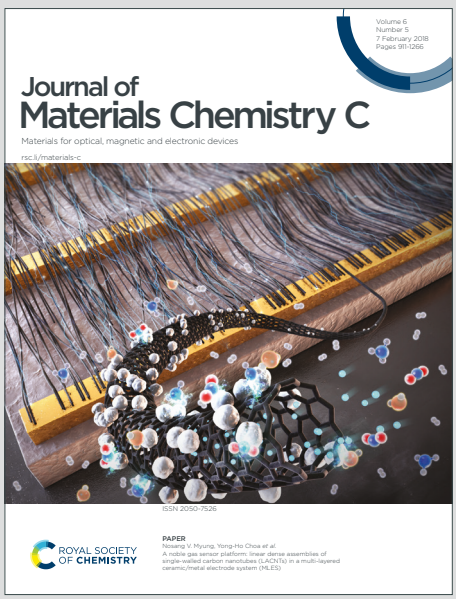

ROYAL SOCIETY OF CHEMISTRY

rsc.li/materials-c

View Article Online
DOI: 10.1039/D4TC01386G

Stabilizing Cubic γ-Ga_2O_3:Cr^{3+} Spinel Nanocrystals by Size Confinement into Mesoporous Silica Nanoreactor Channels

Michele Crozzolin,[1] Camilla Belloni,[1] Jian Xu,[2,3] Takayuki Nakanishi,[4] Jumpei Ueda,[5] Setsuhisa Tanabe,[3] Federico Dallo,[6] Eleonora Balliana,[7] Asia Saorin,[1] Flavio Rizzolio,[1,8] Davide Cristofori,[1] Pietro Riello,[1] Alvise Benedetti,[1] Michele Back,[1,*]

[1] Department of Molecular Sciences and Nanosystems, Ca' Foscari University of Venice, Via Torino 155, 30172, Mestre – Venezia, Italy

[2] International Center for Young Scientists (ICYS), National Institute of Materials Science (NIMS), Tsukuba, Ibaraki 305-0044, Japan

[3] Graduate School of Global Environmental Studies, Kyoto University, Yoshida nihonmatsu-cho, Sakyo-ku, Kyoto 606-8501, Japan

[4] Advanced Phosphor Group, National Institute of Materials Science (NIMS), Tsukuba, Ibaraki 305-0044, Japan

[5] Graduate School of Advanced Science and Technology, Japan Advanced Institute of Science and Technology (JAIST), 1-1 Asahidai, Nomi, Ishikawa, 923-1292 Japan

[6] Institute of Polar Sciences - National Research Council (ISP-CNR), Via Torino 155, 30172, Venezia-Mestre, Venice, Italy

[7] Department of Environmental Sciences, Informatics, Statistics, Ca' Foscari University of Venice, Scientific Campus - Via Torino 155, 30170 Venezia Mestre, Italy

[8] Pathology Unit, Department of Molecular Biology and Translational Research, Centro di Riferimento Oncologico di Aviano (CRO) IRCCS, via Franco Gallini 2, 33081 Aviano, Italy

* corresponding author email: michele.back@unive.it

Abstract

In recent years, Cr^{3+}-activated phosphors have been attracting a lot of interest due to their unique optical features exploited for applications ranging from lasers to optical thermometry, near-infrared (NIR) emitting phosphors for bioimaging and NIR-LEDs, to name a few. Despite the interesting optical properties shown by Cr^{3+} into Ga_2O_3, investigations are limited only to the β-Ga_2O_3 and α-Ga_2O_3 polymorphs. Using mesoporous silica particles with different pore sizes between 3 nm and 22 nm as nanoreactors, cubic γ-Ga_2O_3:Cr^{3+} spinel nanocrystals (NCs) are stabilized through the confinement into the mesopores as confirmed by HR-TEM, XRPD and the photoluminescence spectral shape. A detailed spectroscopic investigation in a temperature range between 16 to 500 K allowed to extrapolate the fundamental parameters in the framework of the Tanabe-Sugano diagram and to compare the values for Cr^{3+} in γ-Ga_2O_3 with the α- and β-phases. In addition, due to the confinement of the NCs into the silica structure, the phase transition to the β-phase, conventionally occurring at about 700 °C, is hindered up to 1000 °C, improving the stability of the γ-Ga_2O_3 phase.

View Article Online
DOI: 10.1039/D4TC01386G

INTRODUCTION

Since the discovery of the ruby laser by Maiman [1], Cr^{3+}-doped crystals have been among the most investigated transition metal ions doped phosphors. The flexibility of the optical properties of Cr^{3+} ions arising from the possibility to control the relative energy level position of the low lying $^4T_2$ and ^2E excited states through the bond lengths and symmetry of the octahedral site of the host, has led a huge interest in developing new Cr^{3+}-doped phosphors for a wide variety of applications. The demonstration of the potentials of Cr^{3+} ions into persistent luminescent materials such as the spinel $ZnGa_2O_4$ [2,3], garnets (e.g. $Y_5Al_{3-x}Ga_xO_{12}$ [4-6]) and perovskite $LaAlO_3$ [7] triggered their investigation for biological applications. In addition, Cr^{3+}-activated phosphors were also demonstrated to be particularly promising as luminescent thermometers based on the ratio between the emissions originated from the spin allowed $^4T_2 \rightarrow {}^4A_2$ and the spin forbidden $^2E \rightarrow {}^4A_2$ transitions [8-12], being proposed for a wide range of temperatures ranging from the cryogenic ($CaHfO_3:Cr^{3+}$ [13]) to high temperatures ($ZnGa_2O_4:Cr^{3+}$ [14]). The customization of the working temperature range is due to the possibility to modulate the relative energy gap between the $^4T_2$ and ^2E states by playing on the octahedral site through the selection of specific host composition and structure [15]. On the other hand, due to the high stability and efficiency of ruby (α-$Al_2O_3:Cr^{3+}$) used as pressure sensor for the diamond anvil cell experiments all over the world [16-18], Cr^{3+}-doped phosphors were also deeply investigated to discover pressure sensors with higher sensitivities [19-21]. More recently, the commercialization of near infrared (NIR) emitting phosphor-converted LEDs based on Cr^{3+}-doped phosphors by Osram, has driven a lot of interest in the development of novel NIR Cr^{3+}-based phosphors characterized by broadband $^4T_2$ emission in weak crystal fields for applications ranging from food and medicines quality monitoring to bioimaging, night vision and plants growth [22-24]. From this perspective, the exploration of novel phosphors activated by Cr^{3+} ions remains highly active.

Gallium oxide (Ga_2O_3) is emerging as one of the most important materials for a variety of technological applications [24]. Ga_2O_3 is a semiconductor capable of adopting various crystallographic structures, with six different polymorphs known: the stable β-phase and five metastable phases α, γ, δ, ε, and κ [25,26]. Among them, β-Ga_2O_3 has been demonstrated to be a promising host for Cr^{3+}-activated phosphors [27-31] being investigated for lasing [28], optical thermometry [15] and pc-NIR LEDs [32]. A detailed spectroscopic investigation on Cr^{3+} ions in the rhombohedral α-Ga_2O_3 phase was recently reported, showing a stronger crystal field with respect to β-Ga_2O_3 [15]. In addition, the corundum-type α-$Ga_2O_3:Cr^{3+}$ system was also proposed as pressure sensor [33]. The Al_2O_3-Ga_2O_3 and Sc_2O_3-Ga_2O_3 solid solutions were also deeply investigated as promising hosts for Cr^{3+} ions [34,35].

The crystalline structure of γ-Ga_2O_3 polymorph was widely investigated and debated due to the complicated defect $Fd\bar{3}m$ spinel structure [36-40]. The γ-Ga_2O_3 stabilization was also proved in glassy hosts [41] showing photocatalytic and catalytic activity [42-44]. The defects present in the γ-Ga_2O_3 spinel structure were exploited to develop size-tuneable luminescent nanocrystals [45] and white-light-emitting nanophosphors when coupled through energy transfer with orange-red emitting organic dyes [46]. Despite the interest in Ga_2O_3 polymorphs as hosts for luminescent centres, a detailed investigation on the Cr^{3+} optical properties in the cubic γ-Ga_2O_3 is still missing.

In this study, we investigate the stabilization of Cr^{3+}-doped γ-Ga_2O_3 nanocrystals (NCs) by taking advantage of the size effect in mesoporous silica particles (MSPs) of different pores size. The effect of the size, and temperature were investigated by means of a series of physical chemical investigation using XRPD, SEM/HR-TEM, N_2 physisorption and TG-DSC analysis. In addition, the

View Article Online
DOI: 10.1039/D4TC01386G

photoluminescence (PL) spectral analysis of Cr^{3+} into the Ga_2O_3 NCs allowed a detailed spectroscopic investigation to probe the crystalline structure. The HR-TEM analysis confirmed the stabilization of the cubic γ-Ga_2O_3 spinel structure. Moreover, a detail investigation of the photoluminescence (PL) and PL excitation (PLE) spectral analysis and the temperature dependence of the PL spectra led to compare the spectroscopic feature of Cr^{3+} with respect to the β- and α-Ga_2O_3 polymorphs and to investigate the effect of the crystal on the $3d^3$ electrons of Cr^{3+} in terms of Tanabe-Sugano diagram and configurational coordinate diagram.

RESULTS AND DISCUSSION

Stabilizing γ-Ga_2O_3 Polymorph by Size: MSPs Pore Effect.

The most common Ga_2O_3 polymorphs, α, β and γ, exhibit distinct differences in crystal structures and coordination polyhedra with a direct influence on their stability and synthetic methods. The trigonal α-Ga_2O_3 (space group $R\bar{3}c$) is characterized by a corundum structure with only octahedral GaO_6 sites, while β-phase by a monoclinic structure (space group $C2/m$) with mixed coordination of octahedral GaO_6 and tetrahedral GaO_4 sites with a ratio 1:1 and the cubic γ-phase (space group $Fd\bar{3}mZ$) by a defective spinel structure with both octahedral and tetrahedral sites characterized by high degree of disorder [36-40]. The unit cell volume increases by moving from the compact β-Ga_2O_3 (~209 $Å^3$) to α-Ga_2O_3 (~289 $Å^3$) and finally to the defective γ-Ga_2O_3 (~559 $Å^3$).

With the aim of investigating the suitable sizes to stabilize the cubic γ-Ga_2O_3 phase, mesoporous silica particles with different mesopores were firstly synthesized as nanoreactors and subsequently the Cr^{3+}-doped Ga_2O_3 nanocrystals were grown by means of an impregnation procedure followed by thermal treatment (Scheme 1).

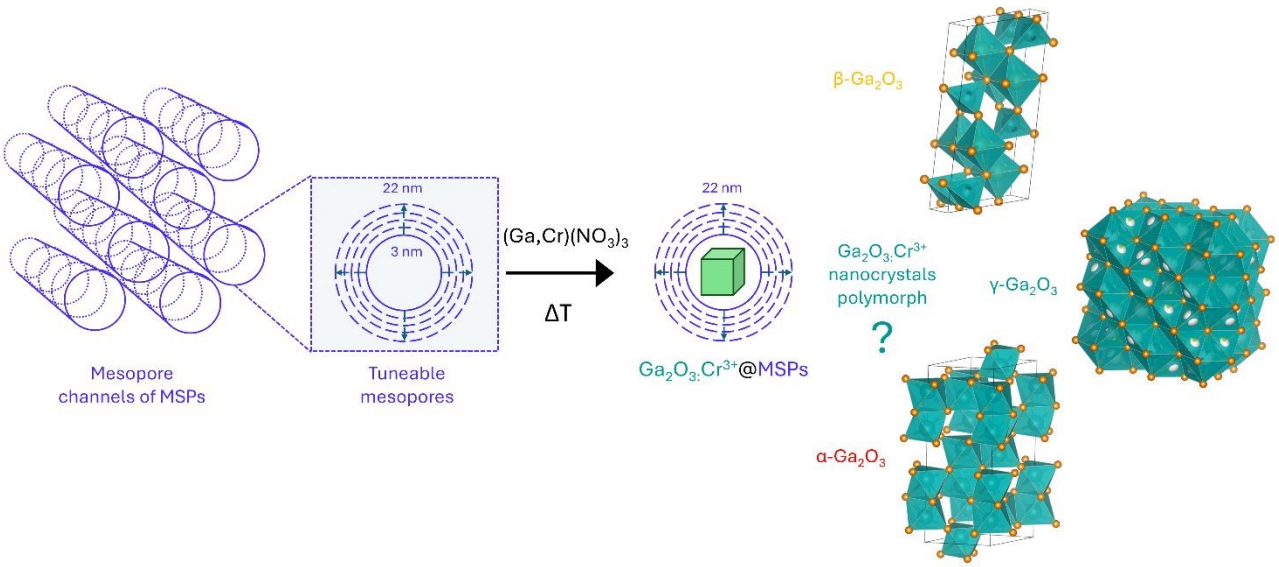

Scheme 1. Sketch of the synthetic procedure for the synthesis of Ga_2O_3:Cr^{3+} nanocrystals with tunable size inside the mesopores of MSPs by means of a wet impregnation strategy followed by thermal treatment and the most common Ga_2O_3 polymorphs that could be stabilized.

View Article Online
DOI: 10.1039/D4TC01386G

MSPs characterized by five different average pore sizes were firstly prepared as shown in **Figure 1a** (labelled as MSP_3.1, MSP_4.2, MSP_7.5, MSP_13.5 and MSP_22.4).

Different synthetic procedures were employed to get access to MSPs characterized by different pore sizes. Spherical MSNs, with an average pore size of 3.1 nm (**Figure 1b**), were obtained following the procedure proposed by Quiao et al. [47]. Spherical MCM-41 MSNs characterized by pore size of 4.2 nm were prepared by means of n-hexane as swelling agent (**Figure 1c**). SBA-15 with average pores of 7.5 nm were synthesized through an aging process in autoclave at 100 °C for 24 hours without the use of swelling agent, while SBA-15 characterized by average pore sizes of 13.5 and 22.4 nm were prepared by using trimethylbenzene at different TMB/Pluronic P123 ratio as swelling agent. The SBA-15 are characterized by the typical hexagonal arranged pore structure morphology (**Figure 1d**, **S1a** and **b**). The conventional tubular shape is lost, and micrometer globular particles are stabilized when TMB/Pluronic P123 ratio of 0.3:1 is employed (**Figure 1e**, **S1c** and **d**). Finally, mesocellular foam with average pore sizes of 22.4 nm were obtained for TMB/Pluronic P123 ratio of 0.5:1 (**Figure 1f** and **S1e** and **f**). The shape evolution is driven by the TMB/Pluronic P123 ratio due to the effect of TMB on the surfactant packing parameter [48]. TMB can be easily dissolved into the PPO core of P123 micelles increasing the volume of the hydrophobic part [49]. This change directly influences the micelle shape, described through the geometric model introduced by Israelachvili [50] by the packing factor $P = V/(a_0 l)$, where V is the total volume of the hydrophobic surfactant chain, a_0 the effective hydrophilic headgroup size and l the kinetic surfactant tail length. When TMB/Pluronic P123 ratio is high ($P > 1$), the need to decrease micelle surface-to-volume ratio leads to micellar aggregates with reverse curvature to be formed [51] and a consequent change in the mesoporous silica structure to mesocellular foam is triggered.

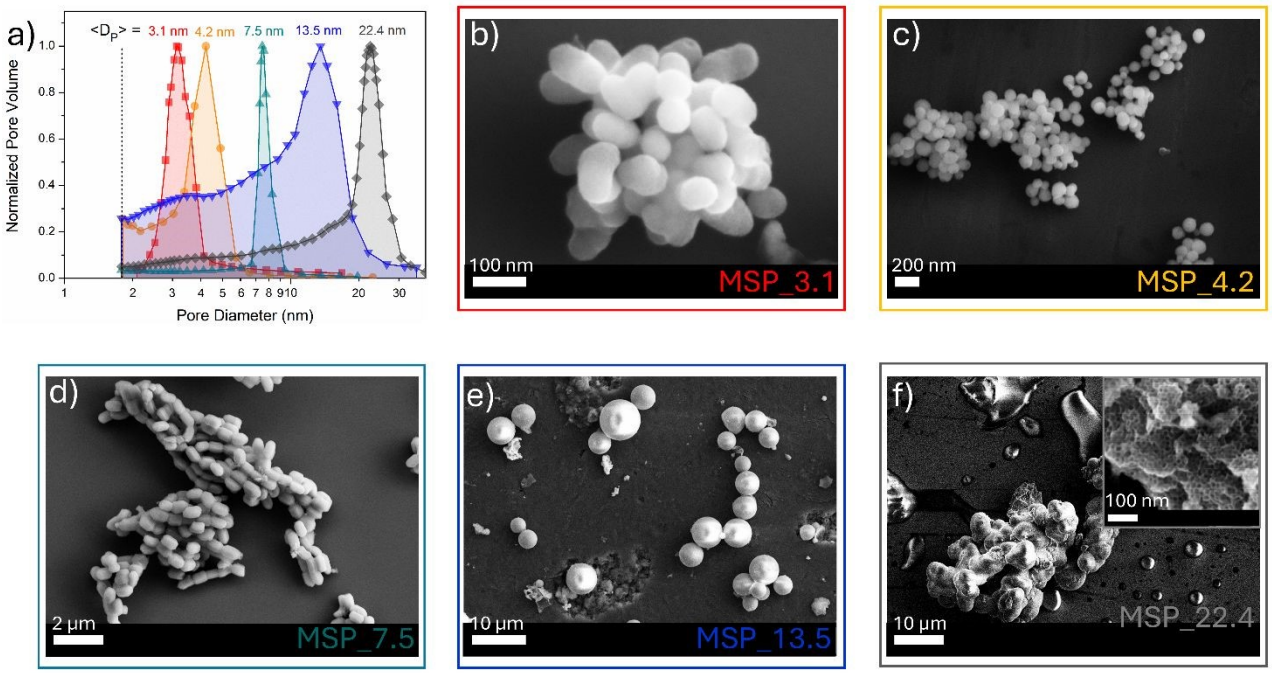

Figure 1. (a) BJH pore size distribution of MSPs and (b-f) corresponding representative FE-SEM images.

View Article Online
DOI: 10.1039/D4TC01386G

The N_2 physisorption analysis allows to estimate the surface area by means of the BET technique (**Table S1**) while the pore size distributions and pore volume of the different MSPs were determined by BJH method (**Figure 1a** and **Table S1**). The N_2 physisorption hysteresis of the MSPs samples are shown in **Figure S2**.

Subsequently, the MSPs were impregnated with Ga/Cr nitrite precursors through a wet impregnation method by fixing the Ga:Cr ratio to obtain a 0.5 at.% doping of the Ga sites in the final target product ($Ga_{1.99}Cr_{0.01}O_3$). After that, the system was thermally treated at 900 °C for 2 hours.

At this stage of the preparation, the XRPD pattern analysis of the samples, shown in **Figure 2a**, independently from the pore size, show a pattern similar to that one of the γ-Ga_2O_3 spinel reference, suggesting the stabilization of the higher symmetric cubic structure. However, the broadening of the diffraction peaks due to the small crystallites and the amorphous contribution of the MSPs make the assignment not unambiguous.

The effectiveness of the impregnation method is demonstrated by the elemental map of Ga inside the MSPs by means of EDX analysis. As shown in **Figure 2b** on the Ga_2O_3:Cr^{3+}@MSP_7.5 sample, as an example, Ga is homogeneously distributed inside the MSPs. In addition, the EDX spectrum allows to confirm the Si, Ga and Cr elements are present in the particles. The elemental maps of Ga, Si and O confirmed the effectiveness of the impregnation irrespective to the pore size as evidenced for instance by the elemental maps for Ga_2O_3@MSP_4.2, Ga_2O_3@MSP_7.5 and Ga_2O_3@MSP_13.5 reported in **Figure S3, S4** and **S5**.

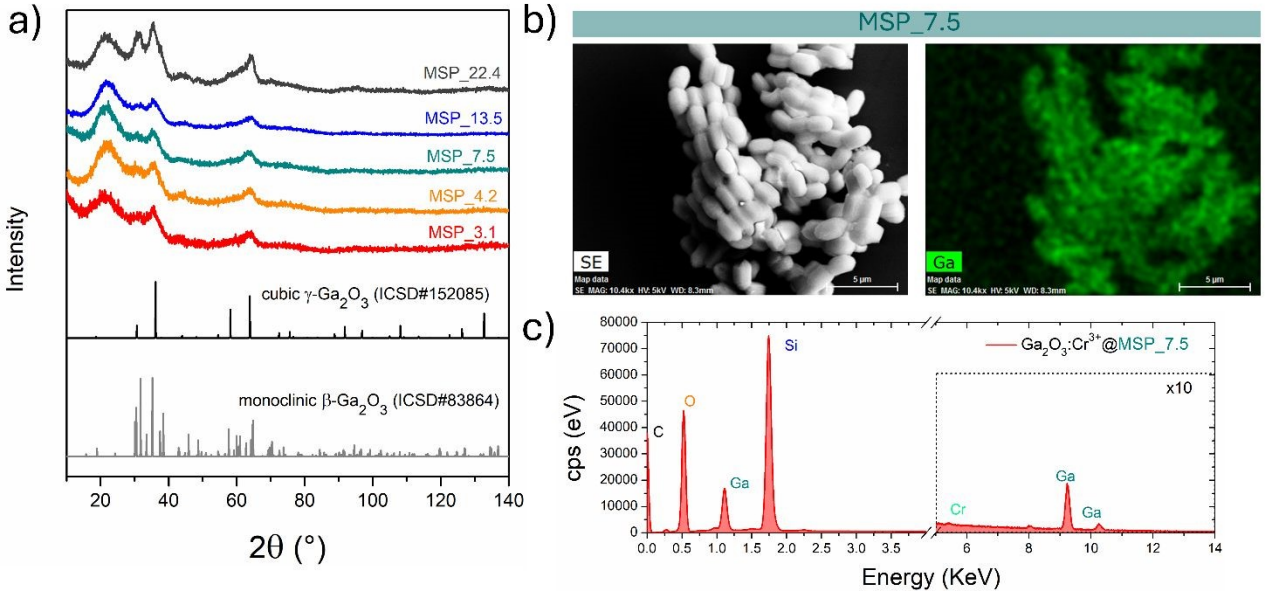

Figure 2. (a) XRPD patterns of the samples with increasing pore size of the mesopores of the MSPs where the Ga_2O_3 NCs were grown. (b) Representative secondary electron-SEM image and corresponding EDX elemental map of Ga and (c) EDX spectrum of Ga_2O_3:Cr^{3+}@MSP_7.5 sample.

To shed light on the phase assignment, Cr^{3+} ions can be used as a structural probe. Indeed, the strong effect of the environment on the optical properties of the $3d^3$ electrons of Cr^{3+} can be used to probe the stabilized polymorphs. In this view, bulk monoclinic β-Ga_2O_3:Cr^{3+} was prepared as reference. The photoluminescence (PL) spectra of Ga_2O_3:Cr^{3+} nanocrystals in **Figure 3a** reveal an unexpected

View Article Online
DOI: 10.1039/D4TC01386G

behavior showing the stabilization of the γ-Ga_2O_3 spinel phase for NCs of 7.5 and 13.5 nm, confirming the XRPD analysis, while at smaller sizes the stable monoclinic β-phase is detected. The PL spectrum of the 22.4 nm sample shows the spectral feature of both the β-phase and γ-phase, suggesting a mixture of the polymorphs. Irrespective to the stabilized phase, the integrated PL area increases linearly with the size of the NCs (**Figure 3b**) evidencing a major role played by the size on the quenching behavior.

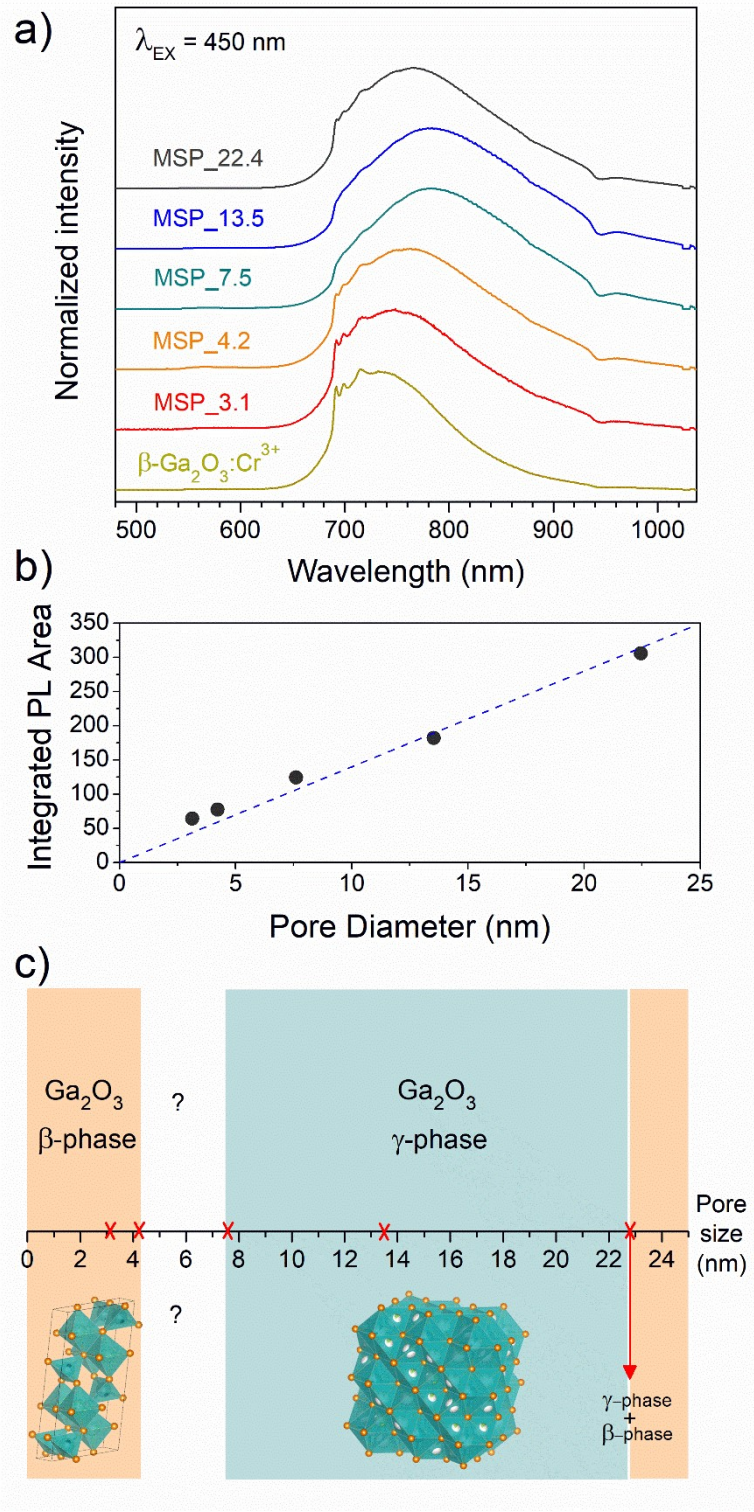

View Article Online
DOI: 10.1039/D4TC01386G

Figure 3. (a) PL spectra of Cr^{3+} in Ga_2O_3 NCs grown in mesopores of different size, (b) integrated PL area as a function of the pore size and (c) diagram of the stabilized Ga_2O_3 polymorph versus pore size.

Figure 3c summarizes the results of the Ga_2O_3 polymorphs stabilization into the mesoporous channels with different size ranges. The stabilization of the cubic γ-Ga_2O_3 phase can be explain by considering the complex interplay between surface energy and bulk thermodynamic stability along with synthesis conditions. The order of phase stability (based on the formation free energy) for the Ga_2O_3 polymorphs is $\beta > \kappa > \alpha > \delta > \gamma$ [52,53]. However, at nanoscale, the surface to volume ratio increases leading the surface energy to play a significant role in the total energy. On the other hand, high-symmetry phases tend to have lower surface energy making γ-phase more favorable at small sizes. The stabilization of higher symmetric structures with the decreasing of the size was already demonstrated for many partially covalent compounds such as CdSe [54,55], ZrO_2 [56], YPO_4, $BaTiO_3$, Al_2O_3, Fe_2O_3, $PbTiO_3$, $PbZrO_3$, $Bi_2CaSr_2Cu_2O_8$ [57], to name a few. With reduction in particle size, a unit cell expansion up to phase transition was demonstrated for these materials, showing an effect similar to the application of a negative pressure [57].

The stabilization of the β-Ga_2O_3 phase for size smaller than 4.2 nm confirms the results reported by Fang et al. [58] and it could be explained considering that the kinetic barriers that need to be overcome to stabilize different polymorphs can be strongly altered by stress and strain, promoting or hindering the stabilization of metastable polymorphs. The same effect of size dependence stabilization of γ- and β-phase was recently demonstrated also for ultrathin Ga_2O_3 nanowires by Wang et al. [59], suggesting that positive or negative strains could inhibit the phase transition to the γ-phase at very small sizes. For sizes larger than about 22 nm, the β-Ga_2O_3 polymorph is again the more thermodynamically favored.

The sample at 7.5 nm was selected as representative of the cubic γ-Ga_2O_3:Cr^{3+}. As evidenced in **Figure S2** and **1a**, the MSP_7.5 sample is characterized by a type H1 hysteresis loop (IUPAC [60]) typical of the SBA-15 and a narrow pore size distribution. The XRPD patterns al low angles of the bare MSP_7.5 shows the characteristic reflections of the (100), (110) and (200) planes of the *p6mm* hexagonally arranged cylindrical pores [61,62] (**Figure 4a**). The well resolved peaks indicate the high degree of hexagonal mesoscopic organization. The intense (100) peak reflects a d spacing of 94 Å, corresponding to a large unit cell parameter $a = 10.9$ nm. After the Ga_2O_3 NCs growth into the MSP channels at 900 °C, the *p6mm* morphology is preserved but the peaks appear at larger 2θ values, with $d_{(100)} = 98$ Å and $a = 9.8$ nm. **Figure 4b** shows the XRPD at higher angles of: the bare SBA-15 MSPs, the SBA-15 MSPs filled with the Ga_2O_3:Cr^{3+} nanocrystals after the thermal treatment at 900 °C and the Ga_2O_3:Cr^{3+} nanocrystals after the MSPs etching by NaOH. The comparison with the Ga_2O_3 polymorphs references evidences the stabilization of the cubic γ-phase. In addition, the theoretical amount of Cr doping was confirmed by ICP-OES analysis. The estimated Ga:Cr=28.62:0.18 shows a doping content of 0.6 at.%, in good agreement with the theoretical value of 0.5% of the Ga sites ($Ga_{1.99}Cr_{0.01}O_3$).

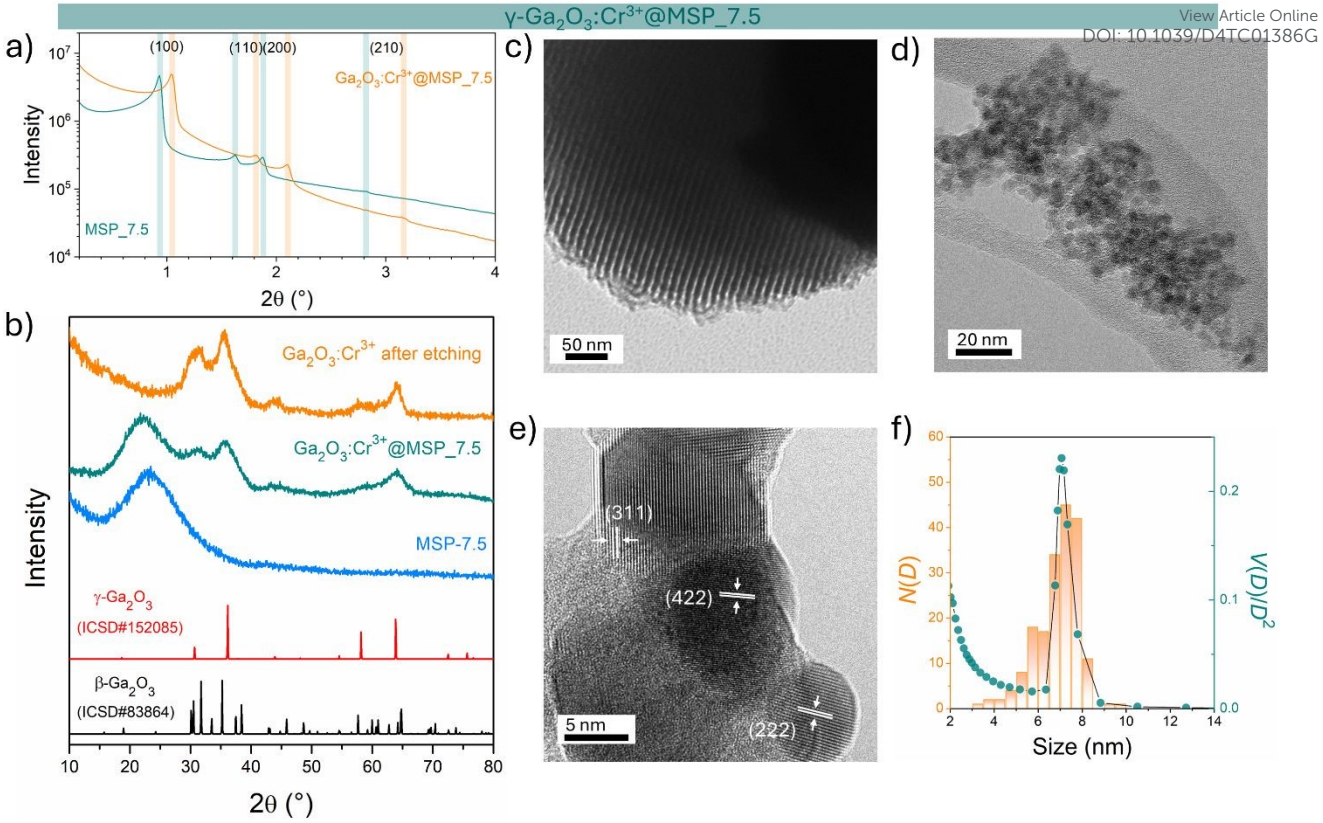

Figure 4. Stabilization of γ-Ga_2O_3 NCs into MSP_7.5: Structural and morphological analysis. (a) XRPD at low angles of the bare MSP_7.5 and the γ-Ga_2O_3@MSP_7.5 sample. (b) Comparison of the XRPD patterns at higher angles of the bare MSP_7.5, Ga_2O_3:Cr^{3+}@MSP_7.5 annealed at 900 °C and the Ga_2O_3:Cr^{3+} NCs etched from the MSP_7.5. TEM images of (c) MSP_7.5 and (d) etched Ga_2O_3 NCs. (e) HR-TEM of the etched Ga_2O_3 NCs together with the *d*-spacing and (hkl) assignment of the crystalline planes. (f) Comparison between the TEM size distribution of the Ga_2O_3 NCs ($N(D)$) with the pore size distribution obtained from BJH ($V(D)/V^2$).

The TEM image of the mesoporous silica MSP_7.5 (**Figure 4c**) shows the well-organized mesopores, as expected by the pore distribution (**Figure 1a**) and the XRPD at low angles (**Figure 4a**). **Figure 4d, S6** and **4e** show the HR-TEM images of the Ga_2O_3 NCs grown into the mesopores of the MSP_7.5 after the etching process. The HR-TEM analysis (**Figure 4e**) provides additional evidence of the stabilization of the cubic γ-Ga_2O_3 polymorph. The images confirm the high crystalline nature of the Ga_2O_3 NCs and the investigation of the *d*-spacing of the families of planes evidenced in the HR-TEM images are unambiguously assigned to the (311), (222), and (422) crystal planes, characteristic of the cubic γ-Ga_2O_3 polymorph (**Table S2**). The very narrow size distribution of the NCs estimated by TEM (numerical distribution, $N(D)dD$) shows a mean value of 6.9 ± 1.0 nm in good agreement with the pore size distribution obtained by BJH method (volumetric distribution, $V(D)dD$ also in this case vary narrow) confirming the stabilization of the γ-Ga_2O_3 NCs inside the pores of the MSP_7.5 (**Figure 4f**). Assuming that the average pore length L is independent of the pore diameter, the two distributions are correlated by $V(D)dD = N(D)\frac{\pi D^2}{4}LdD$ [63], and the $N(D)$ obtained by TEM is compared with $V(D)/D^2$ obtained by BJH.

It is worth noting that if the silica is etched from the Ga_2O_3@MSP system without the use of ultrasonic bath, this nanocasting method leads to a mesoporous γ-Ga_2O_3 replica of the SBA-15 (see **Figure S7**)

View Article Online
DOI: 10.1039/D4TC01386G

with potential applications as support for nanocatalysts or directly as mesoporous catalyst itself [42,43].

The cubic γ-Ga_2O_3 spinel phase is well known to undergo a phase transition to the β-phase at high temperature [39,64,65]. In order to investigate the effect of the silica structure on the phase stability, the effect of a thermal treatment at 1000 °C was studied by comparing the results of a TG-DSC analysis with the XRPD and the PL spectral shape after the annealing.

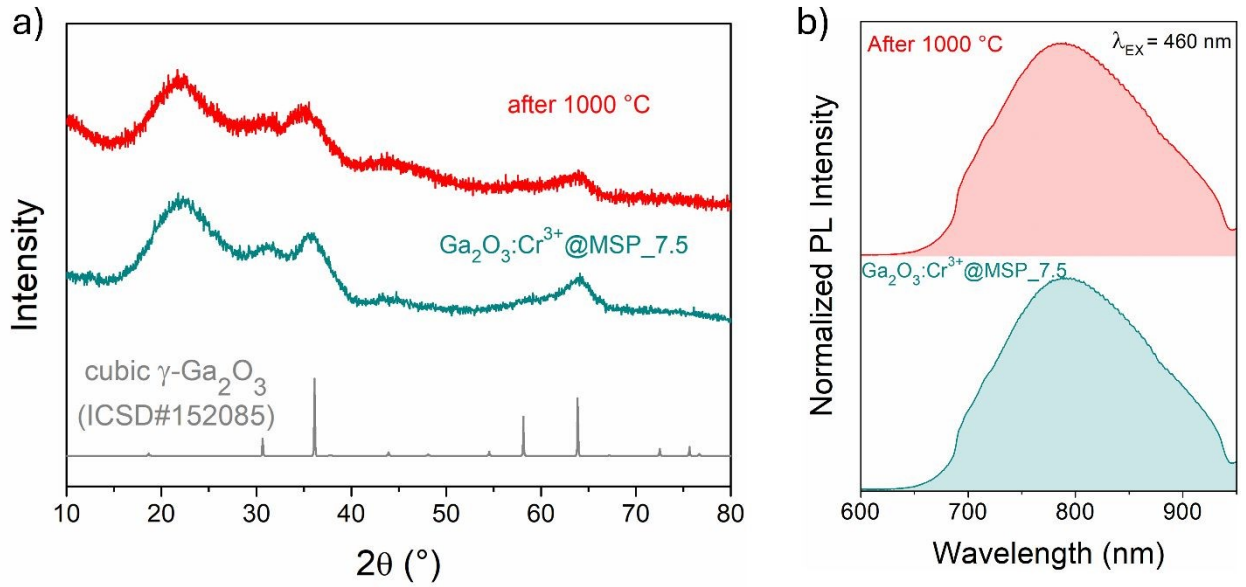

Figure 5. Stability tests up to 1000 °C. (a) XRPD pattern of the sample before and after the TG-DSC analysis up to 1000 °C and (b) corresponding normalized PL spectra obtained exciting at 460 nm.

The TG-DSC analysis on the γ-$Ga_2O_3:Cr^{3+}$@MSP_7.5 system (**Figure S8**) evidences the lack of phase transitions in the range explored, up to 1000 °C and the thermal stability of the system. This is also confirmed by the XRPD analysis and the comparison of the PL spectra of the sample after the treatment. As clearly visible in **Figure 5a** and **b**, the γ-phase is kept suggesting that the phase transformation from γ to β recorded by Castro-Fernandez et al. [39] at 550-750 °C for nanocrystals of about 2.5 nm is influenced by the size. Moreover, the silica structure can also play an important role. However, the stability of the γ-Ga_2O_3 spinel structure up to 1000 °C could be very important for instance for applications in high temperature catalysis.

Spectroscopic Investigation and Thermal Stability of γ-$Ga_2O_3:Cr^{3+}$ Spinel Nanocrystals

In order to investigate the effect of the local crystal site on the $3d^3$ electrons of Cr^{3+}, a spectroscopic investigation is employed. **Figure 6a** shows the PL and PLE spectra of Cr^{3+} in the cubic γ-Ga_2O_3 spinel NCs. The PL spectrum is characterized by a broadband centered at about 792 nm and a FWHM of 2785 cm^{-1} due to the spin allowed $^4T_2 \rightarrow {}^4A_2$ transition, typical of the weak crystal field materials, while the PLE spectrum is composed by the $^4A_2 \rightarrow {}^4T_2$ and $^4A_2 \rightarrow {}^4T_1$ transitions. It is well-known that to better understand the energy levels of transition metal ions in a crystal, the Tanabe-Sugano theory

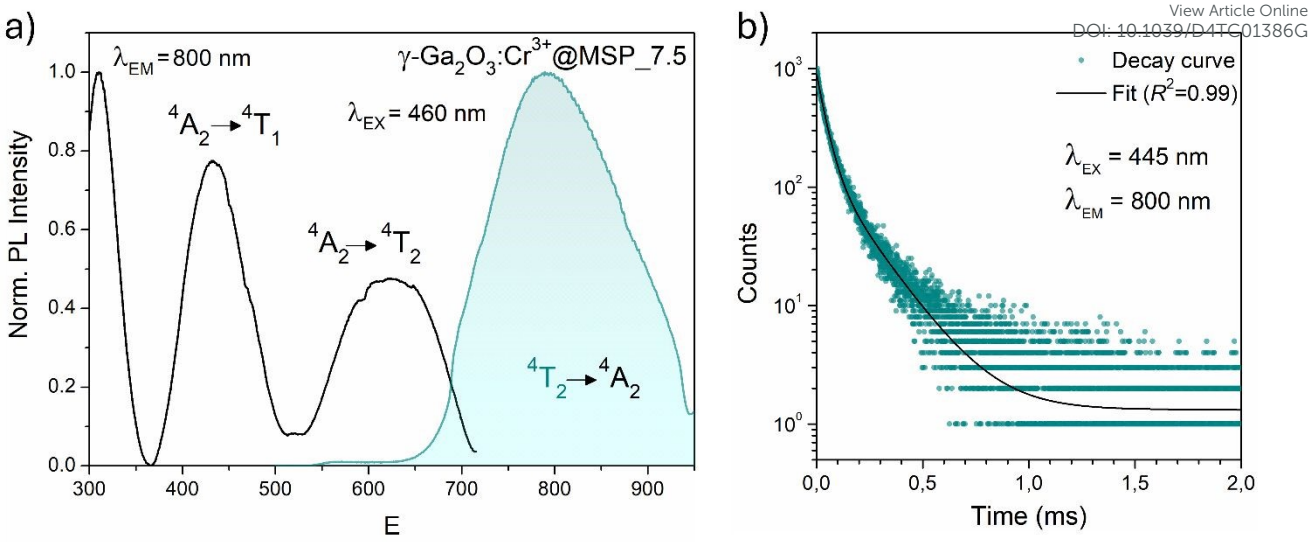

Figure 6. PL and PLE spectra of the γ-Ga_2O_3:Cr^{3+}@MSP_7.5 sample exciting at 460 nm and collecting at 800 nm, respectively. (b) Decay curve exciting at 445 nm and collecting at 800 nm along with the fitting curve.

can be employed [66]. The crystal field strength $10Dq$ and the Racah parameters B and C can be directly estimated from the excitation and emission bands positions:

$$10Dq = E(^4A_2 \rightarrow ^4T_2) \qquad (1)$$

$$\frac{B}{Dq} = \frac{\left(\frac{\Delta E_{4_T}}{Dq}\right)^2 - 10\left(\frac{\Delta E_{4_T}}{Dq}\right)}{15\left(\frac{\Delta E_{4_T}}{Dq} - 8\right)} \qquad (2)$$

$$C \cong \frac{E(^2E)}{3.05} - \frac{7.90B}{3.05} + \frac{1.8}{3.08}\left(\frac{B^2}{Dq}\right) \qquad (3)$$

where $\Delta E_{4_T} = E\left(^4T_{1g}\right) - E(^4T_{2g})$, the difference in energy between the $^4T_{1g}$ and $^4T_{2g}$ states. The energies of the $^4A_2 \rightarrow ^4T_2$ and $^4A_2 \rightarrow ^4T_1$ transition bands were estimated to be 15873 cm^{-1} and 22831 cm^{-1}, respectively. The $10Dq$ and B parameter are therefore calculated to be 15873 cm^{-1} and 720 cm^{-1}, respectively, leading to a Dq/B of 2.2. This value is typical of the weak crystal field and smaller than the corresponding values for the rhombohedral α-Ga_2O_3:Cr^{3+} (2.97 [15]) and monoclinic β-Ga_2O_3:Cr^{3+} (2.58 [15]). In addition, a Stokes shift E_{Stokes} of 3247 cm^{-1} is estimated.

The PL decay curve of the spin-allowed $^4T_2 \rightarrow ^4A_2$ transition of the γ-Ga_2O_3:Cr^{3+} NCs evidences a double-exponential behavior (fitted by $I(t) = I_0 + A_1 e^{-\frac{t}{\tau_1}} + A_2 e^{-\frac{t}{\tau_2}}$, where τ_i and A_i are the decay times and the corresponding amplitudes of the decay components) with an average decay time $\tau_{ave} = (A_1\tau_1^2 + A_2\tau_2^2)/(A_1\tau_1 + A_2\tau_2)$ of 40 μs. The behaviour of the decay curve may be explained by considering the difference between the crystallographic sites in the core and the surface of the spinel NCs. In fact, for many oxide nanocrystals, it has been demonstrated that decreasing the size leads to a negative pressure at the surface, resulting in a deformation of the unit cell with a relative expansion with respect to the "bulk" core (e.g. MgO, CeO_2, Co_3O_4, Fe_3O_4, Cu_2O, Y_2O_3 and $BaTiO_3$ [67-71]);

View Article Online
DOI: 10.1039/D4TC01386G

stronger bonding at the core and a relaxation at the surface [71,72]. Therefore, Cr^{3+} ions could be stabilized in two slightly different octahedral sites of the same γ-phase, at the core and the surface of the NCs, reflecting the bi-exponential behaviour of the decay curve. However, the lifetime estimated is consistent with the conventional microseconds' lifetimes of the $^4T_2$ excited state of Cr^{3+} ions. It is worth noting that recently, Zhao et al. reported a persistent luminescence behaviour in γ-Ga_2O_3:Cr^{3+} by co-doping with Ba^{2+} [73].

To fairly compare the effect of the environment of different compounds on the Cr^{3+} electrons, the Tanabe-Sugano diagram calculated for the specific *C*/*B* should be considered. To calculate the Racah parameter *C*, the ^2E transition is necessary. However, it is not clearly visible in the RT spectra. The low temperature PL spectrum was measured at 16 K (**Figure 7a**). The peaks at 14500 cm^{-1} and 14365 cm^{-1} were assigned to the $^4T_2$ zero phonon line (ZPL) and the ^2E, respectively (**Figure 7b**). With the R-line value, the *C* parameter was calculated to be 3035 cm^{-1} and *C*/*B*=4.21. **Figure 7c** shows the Tanabe-Sugano diagram calculated for the specific *C*/*B* value.

Figure S9 shows the comparison of the PL and PLE spectra of Cr^{3+} in the γ-Ga_2O_3, β-Ga_2O_3 and α-Ga_2O_3 polymorphs, while **Table 1** summarized the main parameters estimated.

Table 1. Comparison of the 10*Dq*, *B*, *C*, *Dq*/*B*, *C*/*B*, <Ga-O> and T_{50} parameters for the different α-, β- and γ-Ga_2O_3:Cr^{3+} polymorphs.

Phase	10*Dq* (cm^{-1})	*B* (cm^{-1})	*C* (cm^{-1})	*Dq*/*B*	*C*/*B*	<Ga-O> (Å)	T_{50} (K)	Ref.
γ	15873	720	3035	2.20	4.21	2.059	415	This work
β	16529	641	3187	2.58	4.97	2.012	480	[15]
α	16393	552	3382	2.97	6.13	1.999	580	[15]

By considering the γ-Ga_2O_3 spinel structure characterized by the cubic $Fd\bar{3}mZ$ space group reported by Zinkevich et al. [36] (ICDS#152085), a single GaO_6 octahedral site with an average <Ga-O> bond length of 2.0595 Å is present. The trends of the Dq/B parameter along with the Racah parameters B and C and therefore C/B can be explained taking into account the difference in the average <Ga-O> bond length of the octahedral site of the polymorphs. Weaker the bond (larger average <Ga-O>) large the parameter *B* and smaller *Dq*/*B* and *C*/*B*.

View Article Online
DOI: 10.1039/D4TC01386G

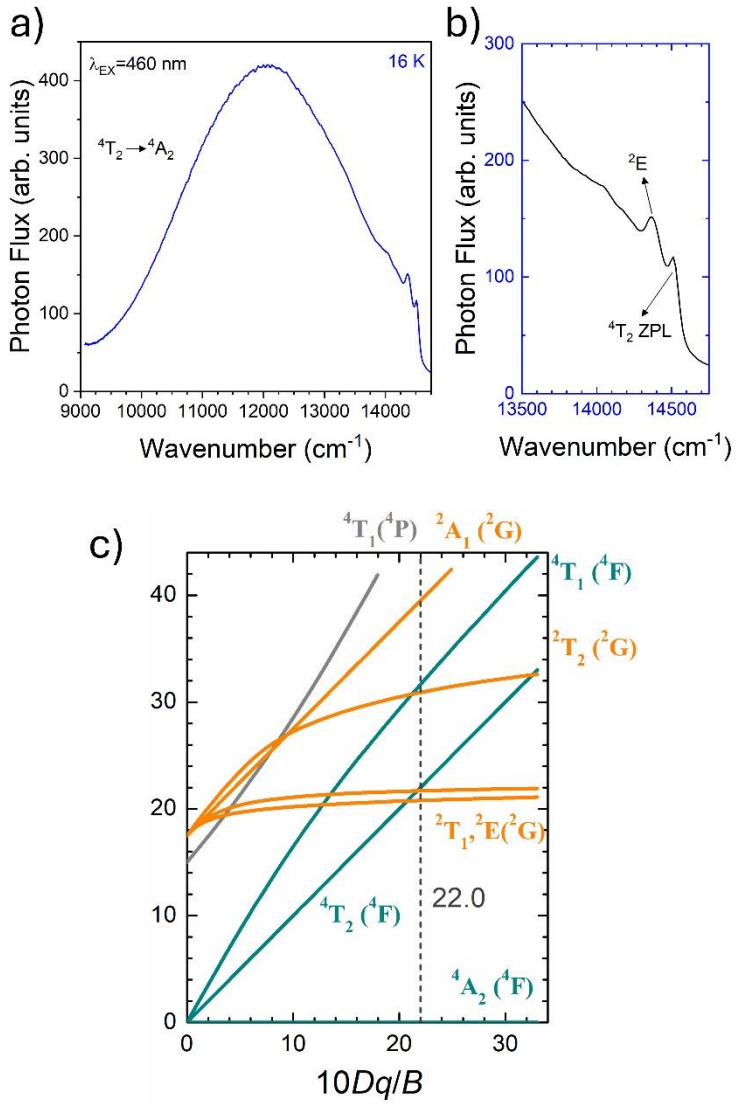

Figure 7. (a) PL spectrum at 80 K collecting at 800 nm and (b) magnification of the (A) $^4T_2$ zero phonon line and ^2E peaks, in the energy scale. (c) Tanabe-Sugano diagram calculated for Cr^{3+} in γ-Ga_2O_3 calculated considering *C*/*B* of 4.21.

The temperature dependence of the PL spectra was investigated in the 16-500 K range (**Figure 8a**). The integrated PL intensity as a function of temperature cannot be reproduced by the simple crossover quenching process described by Struck and Fonger model [74]. As for the case of Eu^{2+}- [75,76] or Bi^{3+}-doped [77] phosphors, a double quenching barrier model is employed:

$$I(T) = \frac{I_0}{1 + A_1 \exp\left(-\frac{\Delta E_1}{k_B T}\right) + A_2 \exp\left(-\frac{\Delta E_2}{k_B T}\right)} \qquad (4)$$

where I is the PL intensity, $A_i = \Gamma_{0,i}/\Gamma_{v,i}$ with $\Gamma_{v,i}$ the radiative rate and $\Gamma_{0,i}$ the attempt rate of the nonradiative process, ΔE_i the activation energy of the quenching processes, k_B is the Boltzmann constant and T is the temperature.

View Article Online
DOI: 10.1039/D4TC01386G

The two energy barriers can be associated to the $^2E \rightarrow {}^4A_2$ (ΔE_1) and $^4T_2 \rightarrow {}^4A_2$ (ΔE_2) thermal quenching at lower and higher temperatures, respectively. From the fitting curve, the ΔE_1 activation energy was estimated to be 83 ± 11 cm^{-1}, in agreement with the small energy difference between the ^2E and the $^4T_2$ ZPL (~135 cm^{-1}) evidenced in **Figure 8b**. On the other hand, a value of 1590 ± 63 cm^{-1} was estimated for the ΔE_2 activation energy related to the $^4T_2 \rightarrow {}^4A_2$ thermal quenching.

In addition, the temperature at which the intensity of the $^4T_2 \rightarrow {}^4A_2$ transition becomes 50% of that one at low temperature, T_{50}, is estimated to be 415 K. Comparing this value with that one estimated for the α-Ga_2O_3:Cr^{3+} (580 K [15]) and β-Ga_2O_3:Cr^{3+} (480 K [15]) polymorphs, a clear trend is evidenced. Indeed, larger the average <Ga-O> bond length of the octahedral site, lower the T_{50}.

The energetic distance $\Delta E'$ between $^4T_2$ and ^2E electronic manifolds obtained for fixed position of ligand ions at the minimum energy of the ^2E parabola can be calculated as the sum of the energy difference ΔE between the minimum energy of the $^4T_2$ and ^2E states and the $S\hbar\omega = E_{Stokes}/2$ energy: $\Delta E' = E_T^0 - E_E^0 = \Delta E + S\hbar\omega$ [78]. By considering this lattice relaxation energy $S\hbar\omega$, in the framework of the perturbation approach and adiabatic approximation [78, 9], the configurational coordinate diagram is depicted in Figure 7c by describing the ground state $^4A_2$ and the excited states ^2E and $^4T_2$ as single parabolic potential curves [79]

$$E_A(\mathrm{Q}) = \frac{\mathrm{Q}^2}{2} \qquad (5)$$

$$E_E(\mathrm{Q}) = \frac{\mathrm{Q}^2}{2} + E_E^0 \qquad (6)$$

$$E_T(Q) = \frac{\mathrm{Q}^2}{2} - \sqrt{2S\hbar\omega}\mathrm{Q} + E_T^0 \qquad (7)$$

where Q represents the configurational coordinate (distance between Cr^{3+} and oxygen ions).

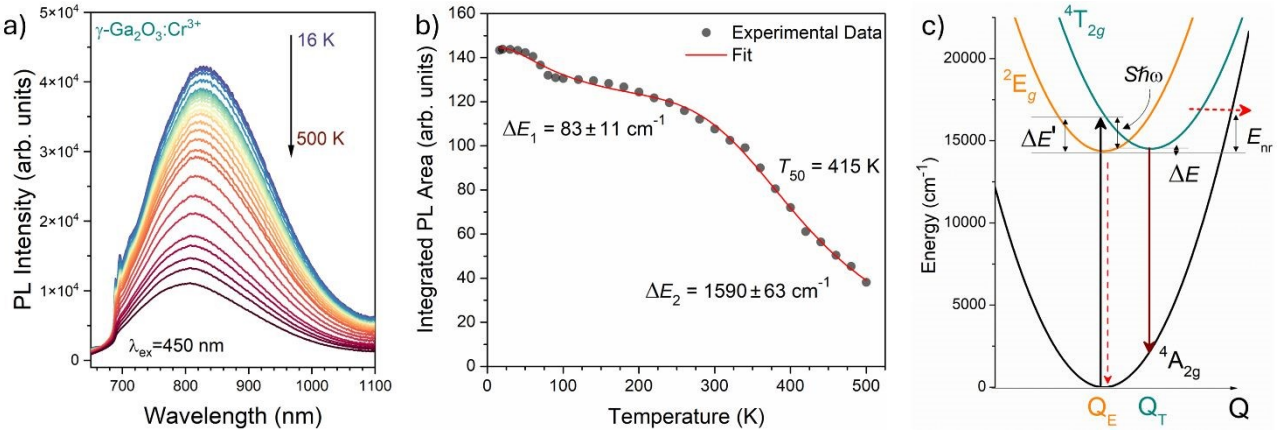

Figure 8. (a) Temperature dependence of PL emission spectra of γ-Ga_2O_3:Cr^{3+} NCs from 16 to 500 K(T). (b) Temperature dependence of integrated PL intensity (black dots) and fit (red curve). (c) Configurational coordinate diagram constructed by using Equations (5)-(7).

View Article Online
DOI: 10.1039/D4TC01386G

The configurational coordinate diagram confirms the very close position between the ^2E and the $^4T_2$ states, in agreement with the Tanabe-Sugano diagram. In addition, the PL spectral features of Cr^{3+} in the three polymorphs shown in **Figure S9** can be explained through the effect of the crystal field on the $3d^3$ electrons of Cr^{3+}: the weaker crystal field in γ-Ga_2O_3 (Dq/B=2.20) leads to the emission only from $^4T_2$, while the intermediate crystal field in β-Ga_2O_3 (Dq/B=2.58) and the stronger field in α-Ga_2O_3 (Dq/B=2.97) lead to emissions from both the $^4T_2$ and ^2E states, with a relative increase of the spin-forbidden $^2E \rightarrow {}^4A_2$ sharp line with respect to the spin-allowed $^4T_2 \rightarrow {}^4A_2$ braodband as the crystal field increases. This trend can also be understood by considering the average <Ga-O> bond length of the octahedral GaO_6 sites in the three polymorphs reported in **Table 1** (the larger the average <Ga-O>, the smaller the Dq/B), in agreement with the multiplet energy level diagram as a function of Cr-O bond length calculated by Ogasawara et al [80]. However, while the shift to a weaker crystal field in the Ga_2O_3 polymorphs leads to a red shift in the spin-allowed $^4T_2 \rightarrow {}^4A_2$ transition, its thermal quenching becomes more severe, being characterized by a smaller T_{50}.

CONCLUSIONS

In conclusion, this study has investigated the stabilization of Cr^{3+}-doped γ-Ga_2O_3 NCs within mesoporous silica particles of various pore sizes. Through a comprehensive physical-chemical analyses including XRPD, SEM/HR-TEM, N_2 physisorption, and TG-DSC, the effects of size and temperature on the stabilization process were thoroughly examined. Spectroscopic analyses further elucidated the crystalline structure, confirming the stabilization of the cubic γ-Ga_2O_3 spinel structure. Moreover, detailed investigations of PL and PLE spectra, alongside temperature dependence studies in the 16-500 K range, provided valuable insights into the spectroscopic characteristics of Cr^{3+} within the γ-Ga_2O_3 matrix in the framework of Tanabe-Sugano theory, allowing the design of the configurational coordinate diagram. A comparison of the properties with respect to the β- and α-Ga_2O_3 polymorphs is provided. Importantly, the use of mesoporous silica particles as nanoreactors effectively stabilized the γ-Ga_2O_3:Cr^{3+} NCs, inhibiting the conventional phase transition to the β-phase up to 1000°C, thus enhancing the stability of the γ-Ga_2O_3 phase.

EXPERIMENTAL

Materials

Chromium nitrate nonahydrate ($Cr(NO_3)_3 \cdot 9H_2O$, 99%), cetyltrimethylammonium bromide ($C_{16}H_{33}N(CH_3)_3Br$, ≥98%), tetraethyl orthosilicate ($Si(OC_2H_5)_4$, 98%), ethanol (EtOH, ≥99.97%), methanol (MeOH, ≥99.9%), n-hexane (C_6H_{12}, ≥99%), Pluronic P-123 and 1,3,5-trimethylbenzene (C_9H_{12}, 98%) were purchased from Sigma-Aldrich. Ammonium hydroxide (NH_4OH, 28-30%) and sodium hydroxide (NaOH, 98%) were purchased from Applichem while gallium nitrate hydrate ($Ga(NO_3)_3 \cdot xH_2O$, 98.9%) from Alfa Aesar.

All the chemicals were reagent grade and used without further purification.

Synthesis of MSPs of different pore sizes

View Article Online
DOI: 10.1039/D4TC01386G

MSPs characterized by average pore size of 3.1 nm (MSP_3.1) were synthesized following the original work reported by Quiao *et al.* [47]. The MSNs were synthesized in a flask thermostated at 60°C using an ionic surfactant for the formation of micelles. 145.2 ml of milliQ water, 5.73 g of cetyltrimethylammonium bromide (CTABr) and 22.8 ml of ethanol are dissolved under vigorous stirring; then 1.25 ml of ammonium hydroxide are added. After about 30 minutes of waiting, 14.6 ml of tetraethoxysilane (TEOS) are added with sustained dripping, then all is left to react for two hours, always with vigorous stirring. Once the synthesis is completed, the MSNs undergo centrifugal deposition cycles at 9000 rpm, elimination of solvent, washing and redispersion by ultrasound in milliQ water until total neutralization of pH. The last washing is carried out in ethanol. After washing, they are placed in an oven at 60°C overnight to evaporate all the solvent, then they are ground in a mortar and calcined at 550°C, with a rate of 2°C/min for 6 hours.

To prepare MSPs with pores a little larger (MSP_4.2), the procedure described by Ma et al. [81] was followed. After solubilization of 0.8 g of CTABr and 3 ml of NaOH 2M in 400 ml of MilliQ water at room temperature, 60 ml of the swelling agent n-hexane was added. After 15 minutes of stirring, the mixture was stopped; then, 4 ml of TEOS were added after separation of phases. The mixture was stirred again for 5 hours, filtered, washed several times with MeOH and dried at 60°C overnight. MSNs were then ground in a mortar and calcined at 550°C, with a rate of 2°C/min for 5 hours.

SBA-15 MSPs with different pore size (MSP_7.5, MSP_13.5 and MSP_22.4) were synthesized following the procedures described in Zhao et al. [61,82] and Cao [83]. This synthesis was carried out in a 250 ml jacketed flask thermostat at 35°C. The preparation takes place by dissolving 4 g of Pluronic P123 block copolymer (polyethylene oxide (EO) - polypropylene oxide (PO) - polyethylene oxide (EO) of formula EO20PO70EO20) in 30 ml of milliQ water and 116.5 ml of HCl 2M. At this point, for MSP_13.5 and MSP_22.4, the swelling agent trimethylbenzene (TMB) was added in 0.3:1 and 0.5:1 w/w rate, respectively. After 30 minutes, 9 ml of TEOS were added with sustained dripping; then the whole mixture was left to react for 20 hours. The suspension was then placed in hermetically sealed Teflon containers in autoclaves for an aging process in oven at 100°C for 24 hours. After cooling to room temperature, the MSNs were washed with deionized water until the pH has been neutralized. The last washing was carried out in ethanol. They were then placed in oven at 100°C for 6 hours in order to evaporate all the solvent and then calcined in a muffle at 550°C.

Impregnation method and γ-Ga_2O_3:Cr^{3+} NCs formation

The precipitation of Ga_2O_3:Cr^{3+} NCs into the MSP mesopores was conducted by incipient wetness impregnation at room temperature. The bare MSNs were dispersed in H_2O, keeping the mixture under stirring. After 30 minutes, the aqueous solutions of the precursor nitrate salts were added in the proper amount to the dispersion with continuous stirring for 2 h. The powder was recovered through the removal of the solvent by means of a rotary evaporator and treated at 900 °C for 2 h.

Silica etching

Silica etching was performed by placing the samples under stirring in a 2M NaOH solution for 2 h. After precipitation, the solvent was eliminated and the Ga_2O_3:Cr^{3+} NCs dried at 60°C overnight.

Bulk α-Ga_2O_3:Cr^{3+} and β-Ga_2O_3:Cr^{3+} references

View Article Online
DOI: 10.1039/D4TC01386G

Gallium nitrate and chromium nitrate solutions were prepared using $Ga(NO_3)_3 \cdot nH_2O$ ($n \cong 7-9$) (99.9%) and $Cr(NO_3)_3 \cdot 9H_2O$ (99.9%). The gallium and chromium solutions were stoichiometrically mixed to obtain $Ga_{0.998}Cr_{0.002}O_3$. In order to precipitate the hydroxide, ammonia solution (28%) was dropped into the mixed solution until the pH reached 6, and then kept stirring for 1 h. The obtained precipitate was separated by a centrifuge and washed by water. The washed product was dried at 100 °C for 2 days and the dried powder was finally treated at 500 °C for 12 h and at 1000 °C for 2 h to obtain α-Ga_2O_3:Cr^{3+} and β-Ga_2O_3:Cr^{3+}, respectively.

Characterizations

Structural and Morphological Analysis

XRPD measurements at high angles were performed by means of a Philips diffractometer with a PW 1319 goniometer with Bragg-Brentano geometry, equipped with a focusing graphite monochromator and a proportional counter with a pulse-height discriminator. Nickel-filtered Cu Kα radiation and a step-by-step technique were employed (steps of 0.05° in 2θ), with a collection time of 30s per step. XRPD measurements at low angles were performed by means of an Empyrean Series 3 (Malvern Panalytical) diffractometer equipped with Cu anode X-ray tube, Bragg-Brentano HD incident-beam optic, and PIXcel^{3D} detector.

Size and morphology determination of the nanoparticles and EDS analysis were carried out with a Carl Zeiss Sigma VP Field Emission Scanning Electron Microscope (FE-SEM) equipped with a Bruker Quantax 200 microanalysis detector, with an accelerating voltage from 5 to 20 kV.

The TEM images were taken at 300 kV with a JEOL 3010 instrument with an ultrahigh resolution (UHR) pole-piece (0.17 nm point resolution), equipped with a Gatan slow-scan CCD camera (model 794) and an Oxford Instrument EDS microanalysis detector (model 6636). The powdered samples were dispersed in isopropyl alcohol solution by sonication and then deposited onto a holey carbon film.

Nitrogen adsorption-desorption isotherms were collected at liquid nitrogen temperature using a Micrometrics ASAP 2010 system. Each sample was degassed at 130°C overnight before the measurements. The Brunauer-Emmett-Teller (BET) equation was used to calculate the specific surface area from the adsorption data and the Barrett-Joyner-Halenda (BJH) model was used to estimate the pore-size distribution from the adsorption branches of the isotherms.

The determination of Gallium (Ga) and Chromium (Cr) concentrations was conducted using Inductively Coupled Plasma Optical Emission Spectrometry (ICP-OES). In the procedure, approximately 10 mg of the sample was transferred into a 50 mL polypropylene (PP) tube. The sample was then subjected to mineralization with 20 mL of aqua regia (a mixture of ultra-pure hydrochloric acid and nitric acid in a 3:1 volume ratio) through sonication for 2 hours at 25°C, using a frequency of 40kHz at 80% intensity (CP104 model from CEIA, Arezzo). This step was followed by mechanical stirring overnight at 100 rpm (VDRL 711 Opto-lab, Modena). Subsequently, the mineralized sample was diluted to a final volume of 50 mL using Milli-Q water (with a resistivity of 18 MΩ·cm) and stored at 4°C. Prior to analysis, the sample was further diluted twofold with Milli-Q water. Alongside the samples, a procedural blank was also prepared for comparison. The analysis itself was performed on an iCAP 7000 Plus instrument (Thermo Scientific, Bremen), which is equipped with a glass concentric nebulizer and a cyclonic spray chamber made of glass. The detection of Ga and Cr was executed in axial mode, targeting their emission lines at 283.563 nm and 294.364 nm, respectively. Quantification of these elements was achieved through external calibration using mono-elemental

View Article Online
DOI: 10.1039/D4TC01386G

standard solutions (provided by UltraScientific, Milan). Five replicates of blanks, standards, and sample measurements were taken and averaged.

Thermogravimetric analysis (TGA) and differential scanning calorimetry (DSC) have been performed with a Netzsch STA 409C in air from 30 to 1000 °C at a heating rate of 10 °C/min. The instrument was purged with a mixture of air and N_2 at a 40 mL/min flow rate. The analysis was performed with an alumina crucible for compatibility. Alumina was used for internal calibration. Three replicates were performed for each sample. Data were collected with STA Netzsch software.

Spectroscopic Measurements and Temperature-Dependent Photoluminescence

PL emission and PLE excitation spectra were carried out using a Horiba-Jobin Yvon Fluorolog 3–21 spectrofluorometer. The photoluminescence spectra were collected by exciting the samples by means of a xenon arc lamp (450 W), selecting the excitation wavelength using a double Czerny-Turner monochromator and collecting with a R928 PMT (Hamamatsu) and a QEPro-XR (Ocean Insight). All spectra were recorded at RT under the same conditions.

Time-resolved PL measurements were carried out under excitation at 445 nm using a pulsed SpectraLED (Horiba Scientific) through the Fluorolog-Time Correlated Single Photon Counting system.

The temperature dependence of PL spectra (16-500 K) was investigated with a cryostat (Janis ST-500, Lake Shore Cryotronics., Inc.), exciting with a 450 nm LD and collecting by means of Hamamatsu PMA-12 CCD (C10027-02). All the spectra were calibrated by means of a standard halogen lamp (DH-2000CAL, Ocean Optics) to obtain spectra in the photon flux scale. In addition, the photon flux per constant wavelength interval function, $\phi(\lambda)$, is converted to photon flux per energy interval by using the Jacobian transformation.

Author contributions

All authors discussed and contributed to the interpretation of the results and the final manuscript. M.B. conceived the presented idea. M.B., J.X., P.R. and A.B. planned the experiments. M.C., M.B. and A.S. prepared the samples. M.B., M.C., C.B., J.X., T.N., J.U., F.D., E.B. and D.C. carried out the experiments. M.B. supervise the project. A.B., S.T., T.N. and F.R. helped supervise the project. M.B. wrote the manuscript with support from M.C., P.R. and A.B.

Conflicts of interest

There are no conflicts to declare.

Acknowledgments

Work by M.B. was financially supported by FY2022 JSPS Invitational Fellowships for Research in Japan (S22088) and the CATHENA project funded by the FVG Region POR-FESR 2014-2020 program (CUP: J34I17000010006). This work has benefited from the infrastructural support of the Centre for Trace Analysis (CeTrA) of Ca' Foscari University through the project IR0000032 –

ITINERIS, Italian Integrated Environmental Research Infrastructures System, funded by EU - Next Generation EU, PNRR.

View Article Online
DOI: 10.1039/D4TC01386G

The authors acknowledge Mr. Tiziano Finotto and Dr. Martina Marchiori for the XRPD and absorption/desorption measurements, respectively.

Notes and references

[1] T. H. Maiman, *Nature*, 1960, **187**, 493-494.

[2] T. Maldiney, A. Bessiere, J. Seguin, Eliott Teston, S. K. Sharma, B. Viana, A. J. J. Bos, P. Dorenbos, M. Bessodes, D. Gourier, D. Scherman, C. Richard, *Nature Mater.*, 2014, **13**, 418-426.

[3] A. Bessiere, S. K. Sharma, N. Basavaraju, K. R. Priolkar, L. Binet, B. Viana, A. J. J. Bos, T. Maldiney, C. Richard, D. Scherman, D. Gourier, *Chem. Mater.*, 2014, **26**, 1365-1373.

[4] J. Ueda, P. Dorenbos, A. J. J. Bos, K. Kuroishi, S. Tanabe, *J. Mater. Chem. C*, 2015, **3**, 5642-5651.

[5] Y. Zhuang, Y. Katayama, J. Ueda, S. Tanabe, *Opt. Mater.*, 2014, **36**, 1907-1912.

[6] J. Xu, J. Ueda, Y. Zhuang, B. Viana, S. Tanabe, *Appl. Phys. Express*, 2015, **8**, 042602.

[7] Y. Katayama, H. Kobayashi, S. Tanabe, *Appl. Phys. Express*, 2015, **8**, 012102.

[8] M. Back, E. Trave, J. Ueda, S. Tanabe, *Chem. Mater.*, 2016, **28**, 8347-8356.

[9] M. Back, J. Ueda, M. G. Brik, T. Lesniewski, M. Grinberg, S. Tanabe, *ACS Appl. Mater. Interfaces*, 2018, **10**, 41512-41524.

[10] M. Back, J. Ueda, J. Xu, K. Asami, M. G. Brik, S. Tanabe, *Adv. Optical Mater.*, 2020, **8**, 2000124.

[11] A. Kabanski, M. Ptak, D. Stefanska, *ACS Appl. Mater. Interfaces*, 2023, **15**, 7074-7082.

[12] Z. Ristic, V. Dordevic, M. Medic, S. Kuzman, M. G. Brik, Z. Antic, M. D. Dramicanin, *Opt. Mater.*, 2021, **120**, 111486.

[13] M. Back, J. Ueda, M. G. Brik, S. Tanabe, *ACS Appl. Mater. Interfaces*, 2020, **12**, 38325-38332.

[14] J. Ueda, M. Back, M. G. Brik, Y. Zhuang, M. Grinberg, S. Tanabe, *Opt. Mater.*, 2018, **85**, 510-516.

[15] M. Back, J. Ueda, H. Nambu, M. Fujita, A. Yamamoto, H. Yoshida, H. Tanaka, M. G. Brik, S. Tanabe, *Adv. Optical Mater.*, 2021, **9**, 2100033.

[16] R. A. Forman, G. J. Piermarini, J. D. Barnett, S. Block, *Science*, 1972, **176**, 284-285.

[17] G. J. Piermarini, S. Block, J. D. Barnett, R. A. Forman, *J. Appl. Phys.*, 1975, **46**, 2774-2780.

[18] H. K. Mao, P. M. Bell, J. W. Shaner, D. J. Steinberg, *J. Appl. Phys.*, 1978, **49**, 3276-3283.

[19] M. Back, J. Ueda, H. Hua, S. Tanabe, *Chem. Mater.*, 2021, **33**, 3379-3385.

[20] M. Szymczak, P. Wozny, M. Runowski, M. Pieprz, V. Lavin, L. Marciniak, *Chem. Eng. J.*, 2023, **453**, 139632.

[21] I. Widmann, G. Kinik, M. Jahnig, R. Glaum, M. Schwarz, C. Wustefeld, D. Johrendt, M. Tribus, C. Hejny, L. Bayarjargal, L. Dubrovinsky, G. Heymann, M. Suta, H. Huppertz, *Adv. Funct. Mater*., 2024, 2400054.

[21] R.-J. Xie, *Light Sci. Appl.*, 2020, **9**, 155.

[23] M. Mao, T. Zhou, H. Zeng, L. Wang, F. Huang, X. Tang, R.-J. Xie, *J. Mater. Chem. C*, 2020, **8**, 1981-1988.

[24] G. N. A. De Guzman, M.-H. Fang, C.-H. Liang, Z. Bao, S.-F. Hu, R.-S. Liu, *J. Lumin.*, 2020, **219**, 116944.

[25] S. J. Pearton, J. Yang, P. H. CaryIV, F. Ren, J. Kim, M. J. Tadjer, M. A. A. Mastro, *Appl. Phys. Rev.*, 2018, **5**, 011301.

[26] R. Roy, V. G. Hill, E. F. Osburn, *J. Am. Chem. Soc.*, 1952, **74**, 719.

[27] H. H. Tippins, *Phys. Rev.*, 1965, **137**, A865.

[28] D. Vivien, B. Viana, A. Revcolevschi, J. D. Barrie, B. Dunn, P. Nelson, O. M. Stafsudd, *J. Lumin.*, 1987, **39**, 29.

[29] C. G. Walsh, J. F. Donegan, T. J. Glynn, G. P. Morgan, G. F. Imbusch, J. P. Remeika, *J. Lumin*., 1988, **40-41**, 103.

[30] Y. Tokida, S. Adachi, *J. Appl. Phys.*, 2012, **112**, 063522.

[31] A. Segure, L. Artus, R. Cuscó, R. Goldhahn, M. Feneberg, *Phys. Rev. Mater.*, 2017, **1**, 024604.

[32] M.-H. Fang, G. N. A. De Guzman, Z. Bao, N. Majewska, S. Mahlik, M. Grinberg, G. Leniec, S. M. Kaczmarek, C.-W. Yang, K.-M. Lu, H.-S. Sheu, S.-F. Hu, R.-S. Liu, *J. Mater. Chem. C*, 2020, **8**, 11013-11017.

[33] H. Yusa, M. Miyakawa, *Inorg. Chem.*, 2024, **63**, 2695-2700.

[34] M.-H. Fang, K.-C. Chen, N. Majewska, T. Lesniewski, S. Mahlik, G. Leniec, S. M. Kaczmarek, C.-W. Yang, K.-M. Lu, H.-S. Sheu, R.-S. Liu, *ACS Energy Lett.*, 2021, **6**, 109-114.

[35] K.-C. Chen, M.-H. Fang, W.-T. Huang, M. Kaminski, N. Majewska, T. Lesniewski, S. Mahlik, G. Leniec, S. M. Kaczmarek, C.-W. Yang, K.-M. Lu, H.-S. Sheu, R.-S. Liu, *Chem. Mater.*, 2021, **33**, 3832-3840.

[36] M. Zinkevich, F. M. Morales, H. Nitsche, M. Ahrens, M. Ruehle, F. Aldiger, *Zeitschrift fuer Metallkunde*, 2004, **95**, 756-762.

[37] H. Y. Playford, A. C. Hannon, E. R. Barney, R. I. Walton, *Chem. – Eur. J.*, 2013, **19**, 2803-2813.

[38] H. Y. Playford, A. C. Hannon, M. G. Tucker, D. M. Dawson, S. E. Ashbrook, R. J. Kastiban, J. Sloan, R. I. Walton, *J. Phys. Chem. C*, 2014, **118**, 16188-16198.

[39] P. Castro-Fernandez, M. V. Blanco, R. Verel, E. Willinger, A. Fedorov, P. M. Abdala, C. R. Müller, *J. Phys. Chem. C*, 2020, **124**, 20578-20588.

[40] L. E. Ratcliff, T. Oshima, F. Nippert, B. M. Janzen, E. Kluth, R. Goldhahn, M. Feneberg, P. Mazzolini, O. Bierwagen, C. Wouters, et al. *Adv. Mater.*, 2022, **34**, 2204217.

View Article Online
DOI: 10.1039/D4TC01386G

[41] N. V. Golubev, E. S. Ignat'eva, V. N. Sigaev, A. Lauria, L. De Trizio, A. Azarbod, A. Paleari, R. Lorenzi, *Phys. Chem. Chem. Phys.*, 2015, **17**, 5141-5150.

[42] R. Lorenzi, N. V. Golubev, E. S. Ignat'eva, V. N. Sigaev, C. Ferrara, M. Acciarri, G. M. Vanacore, A. Paleari, *J. Colloid Interface Sci.*, 2022, **608**, 2830-2838.

[43] Z. Yang, L. X. Song, Y. Q. Wang, M. M. Ruan, Y. Teng, J. Xia, J. Yang, S. S. Chen, F. Wang, *J. Mater. Chem. A*, 2018, **6**, 2914-2921.

[44] P. Castro-Fernandez, D. Mance, C. Liu, I. B. Moroz, P. M. Abdala, E. A. Pidko, C. Copéret, A. Fedorov, C. R. Müller, *ACS Catal*., 2021, **11**, 907-924.

[45] T. Wang, S. S. Farvid, M. Abulikemu, P. V. Radovanovic, *J. Am. Chem. Soc*., 2010, **132**, 9250-9252.

[46] T. Wang, V. Chirmanov, W. H. M. Chiu, P. V. Radovanovic, *J. Am. Chem. Soc*., 2013, **135**, 14520-14523.

[47] Z. A. Qiao, L. Zhang, M. Guo, Y. Liu, Q. Huo, *Chem. Mater*., 2009, **21**, 3823-3829.

[48] C. Xin, N. Zhao, H. Zhan, F. Xiao, W. Wie, Y. Sun, *J. Colloid Interface Sci*., 2014, **433**, 176-182.

[49] T. Lu, X. D. Yao, G. Q. Lu, Y. He, *J. Colloid. Interfaces Sci.* 2009, **336**, 368-373.

[50] J. N. Israelachvili, Intermolecular and Surface Forces, Academic Press, London, 1985.

[51] T. Shimizu, M. Masuda, H. Minamikawa, *Chem. Rev.* 2005, **105**, 1401-1444.

[52] Y. Yoshioka, H. Hayashi, A. Kuwabara, F. Oba, K. Matsunaga, I. Tanaka, *J. Phys.: Condens. Matter* 2007, **19**, 346211.

[53] J. Zhao, J. Byggmastar, H. He, K. Nordlund, F. Djurabekova, M. Hua, *JNpj Comput. Mater.* 2023, **9**, 159.

[54] C. B. Murray, D. J. Norris, M. G. Bawendi, *J. Am. Chem. Soc*., 1993, **115**, 8706-8715.

[55] D. V. Talapin, A. L. Rogach, A. Kornowski, M. Haase, H. Weller, *Nano Lett*., 2001, **1**, 207-211.

[56] R. C. Garvie, *J. Phys. Chem*., 1965, **69**, 1238-1243.

[57] P. Ayyub, V. R. Palkar, S. Chattopadhyay, M. Multani, *Phys. Rev. B*, 1995, **51**, 6135-6138.

[58] M.-H. Fang, T.-Y. Li, W.-T. Huang, C.-L. Cheng, Z. Bao, N. Majewska, S. Mahlik, C.-W. Yang, K.-M. Lu, G. Leniec, S. M. Kaczmarek, H.-S. Sheu, R.-S. Liu, *ACS Energy Lett.*, 2021, **6**, 659-664.

[59] J. Wang, X. Guan, H. Zheng, L. Zhao, R. Jiang, P. Zhao, Y. Zhang, J. Hu, P. Li, S. Jia, J. Wang, *Nano Lett*., 2023, **23**, 7364-7370.

[60] M. Thommes, K. Kaneko, A. V. Neimark, J. P. Olivier, F. Rodriguez-Reinoso, J. Rouquerol, K. S. W. Sing, *Pure Appl. Chem.*, 2015, **87**, 1051-1069.

[61] D. Zhao, J. Feng, Q. Huo, N. Melosh, G. H. Fredrickson, B. F. Chmelka, G. D. Stucky, *Science,* 1998, **279**, 548-552.

[62] M. Kruk, M. Jaroniec, C. H. Ko, R. Ryoo, *Chem. Mater.*, 2000, **12**, 1961-1968.

[63] G. Sponchia, R. Marin, I. Freris, M. Marchiori, E. Moretti, L. Storaro, P. Canton, A. Lausi, A. Benedetti, P. Riello, *J. Nanopart. Res.* 2014, **16**, 2245.

[64] C. Wouters, M. Nofal, P. Mazzolini, J. Zhang, T. Remmele, A. Kwasniewski, O. Bierwagen, M. Albrecht, *APL Mater*., 2024, **12**, 011110.

[65] X. Zhang, H. Huang, Y. Zhang, D. Liu, N. Tong, J. Lin, L. Chen, Z. Zhang, X. Wang, *ACS Omega*, 2018, **3**, 14469-14476.

[66] Y. Tanabe, S. Sugano, *J. Phys. Soc. Jpn.*, 1954, **9**, 766.

[67] S.-W. Chan, W. Wang, *Mater. Chem. Phys.*, 2021, **273**, 125091.

[68] V. Perebeinos, S.-W. Chan, F. Zhang, *Solid State Commun.*, 2002, **123**, 295-297.

[69] G. Kimmel, A. Sahartov, Y. Sadia, Z. Porat, J. Zabicky, E. Dvir, *J. Mater. Res. Technol.*, 2021, **12**, 87-99.

[70] C. Beck, K. H. Ehses, R. Hempelmann, C. Bruch, *Scripta Mater.*, 2001, **44**, 2127-2131.

[71] M. Fukuhara, *Phys. Lett. A*, 2003, **313**, 427-430.

[72] M. Leoni, *Mater. Sci. Forum,* 2004, **443-444**, 1-10.

[73] T. Zhao, R. Abdurahman, Q. Yang, R. Aiwaili, X.-B. Yin, *J. Mater. Chem. C*, 2024, **12**, 498-507.

[74] C. W. Struck, W. H. Fonger, *J. Appl. Phys.*, 1971, **42**, 4515-4516.

[75] P. F. Smet, J. E. Van Haecke, F. Loncke, H. Vrielinck, F. Callens, D. Poelman, *Phys. Rev. B*, 2006, **74**, 035207.

[76] S. Mahlik, K. Wisniewski, M. Grinberg, R. S. Meltzer, *J. Phys.: Condens. Matter* 2009, **21**, 245601.

[77] M. Back, J. Ueda, J. Xu, K. Asami, L. Amidani, E. Trave, S. Tanabe, *J. Phys. Chem. C*, 2019, **123**, 14677-14688.

[78] M. Grinberg, A. Suchoucki, *J. Lumin.*, 2007, **125**, 97-103.

[79] M. Grinberg, T. Lesniewski, *J. Lumin.*, 2019, **214**, 116574.

[80] K. Ogasawara, F. Alluqmani, H. Nagoshi, *ECS J. Solid State Sci. Technol.* 2016, **5**, R3191.

[81] S. Ma, Y. Wang, Y. Zhu, *J. Porous. Mater.*, 2011, **18**, 233-239.

[82] D. Zhao, Q. Huo, J. Feng, B. F. Chmelka, G. D. Stucky, *J. Am. Chem. Soc.*, 1998, **120**, 6024-6036.

[83] L. Cao, T. Man, M. Kruk, *Chem. Mater.*, 2009, **21**, 1144-1153.

The data supporting this article have been included as part of the Supplementary Information.

View Article Online
DOI: 10.1039/D4TC01386G